Electronic, magnetic, optical properties, and morphological characteristics of nanocrystalline based on zinc–cobalt molybdate prepared by soft chemistry route

H Lakhlifi, Y El Jabbar, A Natik, H Lassri, M Abid, L Er-Rakho, Sophie Guillemet-Fritsch, R El Ouatib

Electronic, magnetic, optical properties, and morphological characteristics of nanocrystalline based on zinc–cobalt molybdate prepared by soft chemistry route

H. Lakhlifi[a],* Y. El Jabbar[a], A. Natik[b], H. Lassri[b], M. Abid[b], L. Er-Rakho[a], S. Guillemet-Fritsch[c], R. El Ouatib[a]

[a] LIME, Faculty of Sciences Aïn Chock, Hassan II University, Casablanca, Morocco.
[b] LPMMAT, Faculty of Sciences Aïn Chock, Hassan II University, Casablanca, Morocco.
[c] Institut Carnot CIRIMAT, CNRS Université de Toulouse, 118 route de Narbonne, 31062 Toulouse Cedex 9, France.

* Corresponding author email: lakhlifihind21@gmail.com (Hind Lakhlifi)

Abstract

We report on a simple technique for the preparation of nanocrystalline metal molybdate $Zn_{1-x}Co_xMoO_4$ ($0 \leq x \leq 1$) using the polymeric route. The formation mechanism, homogeneity, and structure of the obtained powders were investigated with thermal analysis (TGA–DTA), X-ray powder diffraction (XRD), and Fourier transform infrared spectroscopy (FTIR). The morphology was examined by scanning electron microscopy (SEM), field emission scanning electron microscopy (SEM–FEG) and Brunauer–Emmett–Teller analysis (BET). The particle size was determined by transmission electron microscopy (TEM). UV–Visible spectroscopy and CIE L*a*b* colorimetric parameters were used for color characterization and measurement. According to the XRD analysis of the obtained compounds, for cobalt content greater than or equal to 45%, the phase formed after grinding is isomorphic to α–$CoMoO_4$. A triclinic phase of zinc molybdate α–$ZnMoO_4$ polycrystals compound is observed for the cobalt content less than or equal to 30%. A triclinic structure of α–$ZnMoO_4$ and monoclinic symmetry of $CoMoO_4$ coexist for cobalt contents between 30% and 45%. The solid solution $Zn_{0.7}Co_{0.3}MoO_4$ **(**ZnCoMo-0.3-600), which was obtained in an acidic environment, was formed of grains of quasi-spherical shape with nanometric sizes between 30 and 100 nm. The specific surface area (BET) of the nanocrystalline powders decrease as a function of the substitution of Co^{2+} in the $ZnMoO_4$, the highest value recorded for the ZnCoMo-0.3-600 powder was about 56.7 m^2g^{-1}. As a result, we can claim clearly from the analysis of the diffuse reflection spectra that the thermochromism occurs from the shift of the $O^{2-} \rightarrow Mo^{6+}$ charge transfer band towards high energies. According to the optical band-gap energy (Eg=2.153 eV), the monoclinic ZnCoMo-1-700 ($CoMoO_4$) was classified as a semiconductor nanomaterial. The theoretical magnetic moment of this sample is approximately $\mu_{theorical}$ = 5.00049 μ_B.

***Keywords**:* A1-Characterization; A1-XRD; A1-Solid solution; B1-Nanomaterials; B2-Semiconductor; B2-Magnetic moment.

1. Introduction

Ternary oxides AB_2O_4 (A= Co, Cu.. and B= Fe, V..) have been selected for their potential of a large use, corresponding to the present and future environmental, economic, scientific, and technological needs, and more particularly the photocatalytic applications [1–3]. Molybdenum-based oxides are very diverse in terms of structural characteristics and physicochemical properties [4]. Additionally, molybdates open the way to various potential technological applications, due to their semiconducting, optical, and optoelectronic properties. These applications include the development of optoelectronic, photo-catalytic, and electrochemical devices [5–8]. The electrochemical performances of $AMoO_4$ materials have been widely exploited for the fabrication of energy storage/conversion devices such as supercapacitors [9,10], hybrid capacitors [11,12], and photoelectrochemical batteries [13,14]. These oxides are also used in optoelectronic systems [15] and in the design of passive optical limiters [16]. Furthermore, they are incorporated into sensors as moisture biosensors [17,18].

Great interest is thus brought to the synthesis of nanocrystalline metals since it is possible to control their physicochemical properties, via the modulation of their structures, sizes, and shapes at the nanometric scale [19]. In the case of metal oxides of the chemical formula $AMoO_4$, it is possible to adjust the physicochemical properties through several parameters such as pressure, temperature, synthesis time, or the concentration and chemical composition of the starting reagents. Recently, in 2017, Ghiyasiyan-Arani et al. [20] investigated the effect of different parameters on the sonochemical synthesis of $FeVO_4$ nanocomposite. The diversity of the synthesis processes (hydrothermal [21–23], microwave irradiation [24,25], Pechini [26,27], sonochemical route [28], solid-solid [29,30], molybdate complexes: ligand loss [31,32] and co-precipitation [33,34]), and preparation conditions (pH, temperature, time...) have a huge influence on the microstructure and morphology of the obtained powders.

Due to its excellent physicochemical properties, $CoMoO_4$ could be considered as an outstanding matrix material for energy storage devices [35,36]. Moreover, due to the combined contributions of cobalt and molybdenum ions, high electrochemical performances could be achieved. However, $ZnMoO_4$ is of much less interest due to its poor electronic conduction [37]. Therefore, attention has been focused on methods for enhancing this material's electrochemical performance [38,39]. Recent studies have shown that transition metal oxides could be favorable for increasing the electrical conductivity and specific

capacitance of materials due to their large specific surface area, structural flexibility, high aspect ratio, and unique mechanical properties [40].

The present study reports on the synthesis and characterization of nanocrystalline metal molybdate $Zn_{1-x}Co_xMoO_4$ ($0 \leq x \leq 1$) using the polymeric route. The effects of the synthesis parameters on the structure, particle size, and morphology were discussed in detail. The ZnCoMo-0.2-700 and ZnCoMo-0.3-700 powders can be applied as a new blue pigment, produced by sol-gel method, in ceramic stains. The origin of the color in these two samples was investigated by UV-visible spectroscopy. Additionally, a theoretical simulations study of the electronic magnetic and optical properties of ZnCoMo-1-700 in relation to both the band structure and the associated projected density of states (PDOS) was performed.

2. Methods and materials

2.1. Synthesis

The synthesis of zinc–cobalt molybdate $Zn_{1-x}Co_xMoO_4$ ($0 \leq x \leq 1$) ultrafine powder began with mixing metal nitrates: zinc nitrate $Zn(NO_3)_2{\cdot}6H_2O$ (98.0%, Sigma Aldrich), cobalt nitrate $Co(NO_3)_2{\cdot}6H_2O$ (99.0%, Sigma Aldrich) and ammonium heptamolybdate $(NH_4)_6Mo_7O_{24}$, $4H_2O$ (99.0%, Acros) in stoichiometric proportions then poured into a solution containing an excess amount of complexing and chelating agents. Citric acid (CA) was then introduced with a molar ratio CA/cations metal of 3. The pH of the obtained solution was adjusted with nitric acid or ammonia. The precursors were obtained after evaporation and drying at 120 °C for 24 hours. These precursors were pre-calcined at 300 °C for 12 hours under air. The black powder obtained was heat treated for 2 hours at temperatures ranging from 600 °C to 800 °C. The composites were denoted as follows;
ZnCoMo-0-T ($ZnMoO_4$, x = 0), ZnCoMo-0.2-T ($Zn_{0.8}Co_{0.2}MoO_4$, x = 0.2), ZnCoMo-0.3-T ($Zn_{0.7}Co_{0.3}MoO_4$, x = 0.3), ZnCoMo-0.35-T ($Zn_{0.65}Co_{0.35}MoO_4$, x = 0.35), ZnCoMo-0.4-T ($Zn_{0.6}Co_{0.4}MoO_4$, x = 0.4), ZnCoMo-0.45-T ($Zn_{0.55}Co_{0.45}MoO_4$, x = 0.45), ZnCoMo-0.6-T ($Zn_{0.4}Co_{0.6}MoO_4$, x = 0.6), ZnCoMo-0.8-T ($Zn_{0.2}Co_{0.8}MoO_4$, x = 0.8) and ZnCoMo-1-T ($CoMoO_4$, x = 1), such as T= temperature of the heat treatment (T= 300, 600, 700, or 800 °C).

2.2. Characterization

The thermal decomposition behaviours of the precursors obtained after pyrolysis were monitored with a DTA–TGA analyser (Apparatus Shimadzu). XRD patterns were obtained at room temperature using a Bruker D_8 employing CuK_α radiation as the X–ray source ($\lambda_{CuK\alpha}$ = 1.5406 Å). The infrared spectra were recorded using an FTIR spectrometer (IR Affinity–1S

Shimadzu). The nanocrystalline metal molybdate solid-solutions were analyzed by Raman spectroscopy using a Horiba Jobin-Yvon HR800 LabRam spectrometer. Data were collected in the range 200–1200 cm^{-1}. The excitation source used was laser irradiation of 516.4 nm wavelength. The morphology and size of the grains were examined with a field emission scanning electronic microscope (JEOL JSM 6700F). A PerkinElmer Lambda 35 UV–Vis spectrophotometer was used to measure diffuse reflectance. The specific surface area of the powders was measured using Brunauer-Emmet-Teller (BET) method by Micrometrics Flowsorb II 2300 instrument. Using a CHROMA METER CR–400/ 410 colorimeter (KONICA MINOLTA), colorimetric measurements were taken in the CIE L*a*b* (Comission Internationale de l'Eclairage's L*a*b* colorimetric system). Theoretical simulations are carried out using the density function theory (DFT) and the full potential linearized augmented plane wave (FP-LAPW) to solve the Kohn-Sham equations. The exchange and correlation energy was calculated using the (GGA-PBE) approximation.

3. Results and discussion

3.1. Thermal decomposition

Thermograms obtained for the ZnCoMo-0.3-300 and ZnCoMo-0.6-300 compounds show similar patterns. The observed weight losses were 69% and 61%, respectively (Fig. 1). For the molybdate ZnCoMo-0.3-300, the thermogram obtained (Fig. 1a) can be divided into several steps: an initial weight loss of ~11.5% is observed between 50 °C and 150 °C, characterized by a very weak endothermic phenomenon that can be attributed to water desorption; a second weight loss of ~57.5% in the temperature range of 300–500 °C, which was accompanied by two exothermic peaks, one located at 425 °C, which would be attributed to organic matter combustion, and the other at 450 °C, which could be due to residual carbon combustion and the beginning of molybdate crystallization; and beyond 500°C, no weight loss was observed, thus, the decomposition was complete.

The thermogram of the ZnCoMo-0.6-300 precursor shows a very slight weight loss of ~5% between 50 and 100 °C, accompanied by endothermic effects, corresponding to dehydration (Fig. 1b). A second weight loss between 300 °C and 530 °C of ~56%, which was characterized by two exothermic peaks, one located at 430 °C, which could be attributed to the combustion of the precursor, the other at 520 °C, which corresponds to the oxidation of the carbon produced during the combustion of the precursor. No phenomena were observed above 550 °C, indicating that the decomposition was complete, which confirms that

temperatures higher than or equal to 600°C are the most appropriate for obtaining phases free of organic residue.

3.2. X–ray diffraction

To study the influence of the cobalt rate on powder crystallization, we prepared samples corresponding to ZnCoMo-x-600 compositions with $0 \leq x \leq 1$ at acidic pH and temperatures of 600, 700, and 800°C. The X–ray diffractograms of these samples after heat treatment showed similar results, we have reported only the results obtained at 600°C (Fig. 2a and Fig. 2b):

* For $0 \leq x \leq 0.3$ compositions, with or without grinding, the powder was monophased and isostructural with triclinic α–$ZnMoO_4$ (φ_T) (ICDD: 01-035-0765).

* For cobalt contents $0.3 < x < 0.45$, without grinding, the X-ray diffractograms show the coexistence of two phases: the triclinic phase (φ_T) and the monoclinic phase (φ_M) isostructural with β–$CoMoO_4$ (ICDD: 00–021–0868) (Fig. 2a). In the case of ground powders, a two-phase mixture was observed: the triclinic phase (φ_T) and the monoclinic phase (φ_M) isostructural with α–$CoMoO_4$ (Fig. 2b).

* For cobalt fractions $x \geq 0.45$, only one phase is observed: either φ_M isostructural with β-$CoMoO_4$, in the case without grinding, or isostructural with α-$CoMoO_4$, in the case of ground powders.

The green α-$CoMoO_4$ (ICDD: 01-073-1331) polymorph was formed by grinding the purple β-$CoMoO_4$ molybdate. The piezochromism phenomenon relates to the color change caused by grinding or pressure in general. The piezosensitive β-$CoMoO_4$ molybdate (ICDD: 00-021-0868) is sensitive to grinding [41]. The representation of the coordination polyhedra is presented in Fig. 2c.

3.3. FTIR and Raman spectroscopy

The identified vibrational modes are classified into two categories, internal modes, which are formed by oscillations inside molecule ionic groups with an immobile center of mass, and external modes, which are vibrations of phonons of the lattice caused by the movement of cations [42]. There are four normal modes: Symmetric stretching vibration (ν_1); symmetric bending (ν_2); antisymmetric stretching (ν_3); and antisymmetric bending vibration (ν_4). The symmetric stretching mode is a singlet, symmetric flexion mode is double, while the two antisymmetric modes triply degenerate under Td. Based on the theoretical group analysis, the

total number of factor group modes due to the regular molybdate MoO_4 tetrahedron is 4 and corresponds to 9 vibrations modes possible in the molybdate compounds. We note that all four modes are Raman active, but only the antisymmetric (T_d) modes are IR active [30,31].

FTIR and Raman spectroscopy studies were carried out on ZnCoMo-0.3-600 and ZnCoMo-0.6-600 nanocrystalline powders, obtained at 600 °C, to confirm the results attained previously (Fig. 3 and 4).

As shown in Fig. 3, the bands at 981, 956, 919, and 904 cm^{-1} are assigned to the antisymmetric stretching of Mo–O in the MoO_4 tetrahedral units, those at 862 cm^{-1} would correspond to the symmetric stretching of O-Mo-O bending vibrations [43–46]. The bands located at 747 and 791 cm^{-1} can be attributed to the extension of the Zn–O–Mo bands [47]. The Zn-O-Mo mode is designated as a wideband system around 650 cm^{-1} [31]. The bands observed at 433 and 435 cm^{-1} are specific to the bending vibration of the Co–O–Mo bands [39]. The peaks in the range of 419 and 418 cm^{-1} originated from the stretching vibration modes of Zn-O-Zn indicating the complete transformation from zinc nitrate to zinc oxide [48].

Fig. 4 also shows the Raman spectra of nanocrystalline powders in the wavelength range of 200–1100 cm^{-1}. Usually, the symmetric stretching modes and antisymmetric stretching modes of MoO_4 tetrahedral units are Raman active and observed in the region 780-960 cm^{-1} [31]. For the ZnCoMo-0.3-600 sample, the symmetric Mo-O (ν1) band could be observed at 957 cm^{-1} and assigned as an intensive singlet in the Raman spectra, the band at 930 cm^{-1} was attributed to the symmetrical stretching modes of the MoO_4 anions [49]. The internal modes ν_3 (antisymmetric stretching, Bg), ν_3 (antisymmetric stretching, Eg), ν_4 (antisymmetric bending, Bg+Eg), ν_4 (symmetric stretching, Bg), and ν_2 (symmetric bending, Ag+Bg) are localized at 871, 852, 804, 358 and 325 cm^{-1} respectively [50]. The weak Raman peak observed at 278 cm^{-1} is attributed to external free rotation mode R (Ag) [51]. For the ZnCoMo-0.6-600 sample, The most high-intensity bands observed at 915 and 878 cm^{-1} correspond to the Mo-O (ν_1 (Ag)) symmetric stretching vibration [52]. Those located at 831 and 787 cm^{-1} are assigned to O-Mo-O antisymmetric stretching vibrations modes [53]. The bands observed at 355 and 318 cm^{-1} were designated to the Mo–O–Co stretching vibrations [54,55]. These results are in good agreement with those obtained from X-ray diffraction and infrared spectroscopic analysis, indicating that cobalt was inserted into the α-$ZnMoO_4$ lattice.

3.4. Morphological properties

The ZnCoMo-0.3-T and ZnCoMo-0.6-T nanocrystalline powders were prepared in acid medium and calcined at 600, 700, and 800 °C for 2 hours and then examined by scanning electron microscopy (SEM) (Fig.5a and Fig.5b). The micrographs obtained show that the analysed powders are formed of particles of various morphologies that are more or less agglomerated. An advanced pre-sintering phenomenon was observed for the powders produced at 800 °C.

For the ZnCoMo-0.3-700 oxide, prepared at acidic pH and calcined at 700 °C for 2 hours, the SEM-FEG images reveal quasi-spherical particles of nanometric size (Fig.5c. (a)). For the powder obtained at 800 °C, the micrograph shows agglomerates of particles, indicating a sintering phenomenon. This is in agreement with the SEM observations (Fig.5c. (b)).

The particle size distribution was calculated by counting the number of particles and measuring their sizes using many SEM images for ZnCoMo-0.3-700 molybdate prepared at acidic pH (Fig. 6). This distribution shows a quasi-Gaussian type profile with a single population of grains ranging in size from 2 to 3 μm.

The particle size of the powder was calculated using transmission electron microscopy. TEM examination was carried out only on the ZnCoMo-0.3-T composition prepared at acidic pH and calcined at 600, 700, and 800 °C. The micrograph obtained for the powder obtained at 600°C indicates that it was formed of more or less individualized quasi-spherical particles with an average size estimated between 30 and 100 nm (Fig. 7a). The TEM micrograph of the powder prepared at 700 °C shows particles more or less spherical but more agglomerated with a nanometric size in the range of 100–160 nm (Fig. 7b). The micrograph of the powder prepared at 800 °C indicates that a pre-sintering takes place with a significant magnification of the grains (crystal growth phenomenon) (Fig. 7c).

The specific surface areas of ZnCoMo-0.3-T and ZnCoMo-0.6-T samples obtained at T= 600, 700 and 800 °C were determined using the BET method. A decrease in specific surface area is shown as a function of annealing temperature (Table 1). In comparison to powders produced at 700, and 800 °C, those obtained at 600 °C have a larger specific surface area. As we observe 56.7 m^2g^{-1} was the highest value recorded for the ZnCoMo-0.3-600 powder. We note that the substitution of Co^{2+} in the $ZnMoO_4$ matrix leads to a decrease in surface area from 56.7 m^2g^{-1} (ZnCoMo-0.3-600) to 42.3 m^2g^{-1} (ZnCoMo-1-600). The value of the specific surface area of the ZnCoMo-1-600 powder is compatible with that obtained by Chen et al. (43.8 m^2 g^{-1}) [56].

With the use of the Scherrer equation, the crystallite size was calculated from the mid-height X-ray diffraction line width measurements made in the angular range of 13.6°–33.6° for ZnCoMo-x-600 ($0 \leq x \leq 1$) molybdates prepared under acidic pH, calcined at 600 °C, and then ground, as shown in Fig. 8. We noticed that the crystallite size decreases abruptly upon the insertion of 30% cobalt and then gradually increases beyond this rate. This drop could be explained by the decrease in the crystallite growth kinetics during the insertion of cobalt into the α-$ZnMoO_4$ matrix. The calculated crystallite size for ZnCoMo-0.3-600 is consistent with that observed under TEM. All microscopic analyses (SEM, FEG-SEM and TEM) show that grain size increases with temperature.

3.5. Effect of pH on morphology

The pH levels of the aqueous solutions of the metal salts and citric acid were adjusted to become acidic or basic by adding nitric acid or ammonia, respectively. The ZnCoMo-0.3-600 and ZnCoMo-0.6-600 powders were characterized by X–ray diffraction. The average crystallite size estimated by the Scherrer's formula from the broadened X-ray diffraction line profiles of ZnCoMo-0.3 and ZnCoMo-0.6 powders increases with pH (Table 2). These molybdates obtained by the calcination of the xerogels prepared at acidic and basic pH levels and calcined at 600 and 700 °C were characterized by SEM (Fig. 9). The SEM micrographs of the powders treated at 600 °C show that they consist of elementary particles of various shapes that are more or less agglomerated. At basic pH, we observed a coarsening of the grains showing pre-sintering characteristics. The SEM images obtained at 700 °C for both compositions under acidic pH show that the powders consist of larger grains than those observed at 600 °C. The micrographs show the advanced pre-sintering characteristics at basic pH. Crystal growth is observed at pH basic, we note that the size and agglomeration of particles increase with pH. These observations are perfectly similar to the results obtained for α-$CuMoO_4$ powder prepared by the sol-gel route [57].

3.6. Optical properties

To illustrate the optical behavior of the ZnCoMo-x-T ($0 \leq x \leq 1$) samples via UV-visible spectroscopy, we chose ZnCoMo-0.3-700 and ZnCoMo-0.6-700 as our study materials (Fig. 10). The blue/violet coloration of the synthesized ZnCoMo-0.3-700 and ZnCoMo-0.6-700 powders is shown in Fig. 10. The diffuse reflectance spectra show the presence of bands in the visible region (400–650 nm). The Co^{2+} ion, located in a distorted octahedral site, is in a strong spin state (weak field) and adopts a $3d^7$ configuration, who's fundamental term is an

orbital triplet: $^4T_1$. It gives rise to the three permitted spin transitions ($\Delta S=0$) $^4T_{1g} \rightarrow {}^4T_{2g}(F)$, $^4T_{1g} \rightarrow {}^4A_{2g}(F)$ and $^4T_{1g} \rightarrow {}^4T_{1g}(P)$. As a result, we can claim clearly from the analysis of the diffuse reflection spectra that the thermochromism occurs from the shift of the $O^{2-} \rightarrow Mo^{6+}$ charge transfer band towards high energies [58,59].

The values of the band gap energy of the ZnCoMo-x-700 ($0 \leq x \leq 1$) solid solutions estimated by extrapolating the linear part of the $(h\upsilon\alpha)^2$ curve as a function of $h\upsilon$ are presented in Table 3. The study by UV-visible absorption spectroscopy showed that these oxides present a direct gap transition (Fig. 11), with a band gap Eg between 4.03 eV for $ZnMoO_4$ and 2.153 eV for β-$CoMoO_4$. The value of the band gap, found at about 2.153 eV (β-$CoMoO_4$), is close to those estimated by Altarawneh et al (1.8 eV) [60] and that of the order of 4.03 eV ($ZnMoO_4$), is in good agreement with the experimental value found by Yadav and Sinha (4.1 eV) [43]. According to these values, we can consider these nanocrystalline oxides as semiconductor materials.

The evolution of the colorimetric parameters L*a*b* of the ZnCoMo-0.2-T and ZnCoMo-0.3-T compounds as a function of temperature is shown in Fig. 12. These evolutions show that the component (-b*) characterizing the blue color, has a maximum at 700°C for compositions ZnCoMo-0.2-700 and ZnCoMo-0.3-700. These powders can be applied as a new blue pigment, prepared by polymeric route, in ceramic stains.

3.7. Electronic, magnetic, and optical properties

Theoretical simulations are carried out using density functional theory (DFT) [61,62] and solving Kohn-Sham equations using the full potential linearized augmented plane wave (FP-LAPW) [63]. The exchange and correlation energy were calculated using the GGA-PBE approximation [64]. Experimental lattice constants were used to investigate the electronic, magnetic, and optical properties of ZnCoMo-1-700 (β-$CoMoO_4$; x=1) as a typical example. The input parameters such as R_{kmax}, G_{max}, and k-point were chosen to be 7, 12, and 200 respectively.

The density of states (DOS) is one of the most important physical quantities for understanding the physical properties of a material. The projected total (DOS) and partial density of states (PDOS) between -8 and 16 are shown in Fig. 13a and 13b, respectively. The Fermi level is taken as the origin of the energies. The analysis of the total and partial density of the state figures of ZnCoMo-1-700 indicates the presence of the band gap, E_g, deducing

that this material has a semiconductor nature. The electronic states are divided into two regions: the first is dominated primarily by Co-d states, with a small contribution from O-p states, and the second is dominated primarily by Co-d and Co-d states, with a small contribution from O-p states.

Fig. 13c illustrates the analysis of the absorption spectrum, which shows the major peaks, called 'critical points'; E_0 is the threshold energy, and E_1 corresponds to the optical gap, which is estimated with respect to the experimental value. Each peak corresponds to an electronic transition; the first three peaks are due to transitions (inter-band) from the valence band to the conduction band.

Extrapolating the linear part of the curve $(\alpha h\upsilon)^2 = f(E)$ until $(\alpha h\upsilon)^2 \rightarrow 0$, the plotting $(\alpha h\upsilon)^2$ as a function of hν gives the value of Eg. This explains perfectly that ZnCoMo-1-700 has the property of a direct band gap. The optical band gap of ~ 1.989 eV was observed (Fig.13d). The calculated value is very similar to that of the experimental results (Fig.11/Table 3). The index of refraction of the ZnCoMo-1-700 system varies as a function of photon energy, as shown in Fig. 13e. The static refractive index of this compound is n(0) = 2.1. In addition, using the experimental lattice constants, the magnetic moments and band gap were determined, as shown in Table 4. A study shows that nanocrystalline metal ZnCoMo-1-700 undergoes a three-dimensional antiferromagnetic transition at TN = 37 K [65].

4. Conclusion

Nanocrystalline metal molybdates ZnCoMo-x-T were synthesized using the polymeric route. The X-ray diffraction analysis of the powders treated at 600, 700 and 800 °C then ground shows two single-phase domains: the triclinic symmetry isotype of α-$ZnMoO_4$ for $0 \leq x \leq 0.3$ compounds and the monoclinic symmetry isotype of α-$CoMoO_4$ for $0.45 \leq x \leq 1$ powders. The resulting powders are formed by single-crystalline elementary particles with a quasi-spherical shape and a size range of 30–160 nm.

Measurements of the colorimetric parameters (L*a*b*) of ZnCoMo-0.3-T and ZnCoMo-0.6-T compositions show that the component (-b*) characterizing the blue color, has a maximum at 700 °C. Based on the optical band-gap energy (Eg=2.153 eV), the monoclinic ZnCoMo-1-700 °C is a semiconductor material. The theoretical magnetic moment of this sample is approximately $\mu_{theorical}$= 5.00049 μ_B.

References

[1] R. Monsef, M. Salavati-Niasari, Electrochemical sensor based on a chitosan-molybdenum vanadate nanocomposite for detection of hydroxychloroquine in biological samples, J. Colloid Interface Sci. 613 (2022) 1–14. https://doi.org/10.1016/j.jcis.2022.01.039.

[2] M. Amiri, M. Salavati-Niasari, A. Pardakhty, M. Ahmadi, A. Akbari, Caffeine: A novel green precursor for synthesis of magnetic $CoFe_2O_4$ nanoparticles and pH-sensitive magnetic alginate beads for drug delivery, Mater. Sci. Eng. C. 76 (2017) 1085–1093. https://doi.org/10.1016/j.msec.2017.03.208.

[3] S.R. Yousefi, H.A. Alshamsi, O. Amiri, M. Salavati-Niasari, Synthesis, characterization and application of Co/Co_3O_4 nanocomposites as an effective photocatalyst for discoloration of organic dye contaminants in wastewater and antibacterial properties, J. Mol. Liq. 337 (2021) 116405. https://doi.org/10.1016/j.molliq.2021.116405.

[4] J. Zheng, C. Xing, Y. Yang, S. Li, H. Wu, Z. Wang, Structure, infrared reflectivity spectra and microwave dielectric properties of a low-firing microwave dielectric ceramic $Pr_2Zr_3(MoO_4)_9$, J. Alloys Compd. 826 (2020) 153893. https://doi.org/10.1016/j.jallcom.2020.153893.

[5] J. Ahmed, M. Ubiadullah, M.A.M. Khan, N. Alhokbany, S.M. Alshehri, Significant recycled efficiency of multifunctional nickel molybdenum oxide nanorods in photo-catalysis, electrochemical glucose sensing and asymmetric supercapacitors, Mater. Charact. 171 (2021) 110741. https://doi.org/10.1016/j.matchar.2020.110741.

[6] A.M. Huerta-Flores, I. Juárez-Ramírez, L.M. Torres-Martínez, J.E. Carrera-Crespo, T. Gómez-Bustamante, O. Sarabia-Ramos, Synthesis of $AMoO_4$ (A = Ca, Sr, Ba) photocatalysts and their potential application for hydrogen evolution and the degradation of tetracycline in water, J. Photochem. Photobiol. Chem. 356 (2018) 29–37. https://doi.org/10.1016/j.jphotochem.2017.12.029.

[7] T. Yang, H. Zhang, Y. luo, L. Mei, D. Guo, Q. Li, T. Wang, Enhanced electrochemical performance of $CoMoO_4$ nanorods/reduced graphene oxide as anode material for lithium-ion batteries, Electrochimica Acta. 158 (2015) 327–332. https://doi.org/10.1016/j.electacta.2015.01.154.

[8] U. Ishrat, Rafiuddin, Preparation and characterization of polystyrene based Nickel molybdate composite membrane electrical–electrochemical properties, J. Saudi Chem. Soc. 20 (2016) S440–S447. https://doi.org/10.1016/j.jscs.2013.01.004.

[9] T. Liu, H. Chai, D. Jia, Y. Su, T. Wang, W. Zhou, Rapid microwave-assisted synthesis of mesoporous $NiMoO_4$ nanorod/reduced graphene oxide composites for high-performance supercapacitors, Electrochimica Acta. 180 (2015) 998–1006. https://doi.org/10.1016/j.electacta.2015.07.175.

[10] J. Bhagwan, Sk.K. Hussain, B.N.V. Krishna, J.S. Yu, Facile synthesis of $MnMoO_4$@MWCNT and their electrochemical performance in aqueous asymmetric supercapacitor, J. Alloys Compd. 856 (2021) 157874. https://doi.org/10.1016/j.jallcom.2020.157874.

[11] L. Gao, G. Chen, L. Zhang, B. Yan, X. Yang, Engineering pseudocapacitive $MnMoO_4$@C microrods for high energy sodium ion hybrid capacitors, Electrochimica Acta. 379 (2021) 138185. https://doi.org/10.1016/j.electacta.2021.138185.

[12] W. Hong, J. Wang, P. Gong, J. Sun, L. Niu, Z. Yang, Z. Wang, S. Yang, Rational construction of three dimensional hybrid Co_3O_4@$NiMoO_4$ nanosheets array for energy storage application, J. Power Sources. 270 (2014) 516–525. https://doi.org/10.1016/j.jpowsour.2014.07.149.

[13] J. Fei, Q. Sun, Y. Cui, J. Li, J. Huang, Sodium carboxyl methyl cellulose and polyacrylic acid binder with enhanced electrochemical properties for $ZnMoO_4 \cdot 0.8H_2O$ anode in lithium ion batteries, J. Electroanal. Chem. 804 (2017) 158–164. https://doi.org/10.1016/j.jelechem.2017.09.061.

[14] A.M. Amanulla, C.M. Magdalane, S. Saranya, R. Sundaram, K. Kaviyarasu, Selectivity, stability and reproducibility effect of CeM - CeO_2 modified PIGE electrode for photoelectrochemical behaviour of energy application, Surf. Interfaces. 22 (2021) 100835. https://doi.org/10.1016/j.surfin.2020.100835.

[15] J.-T. Ren, X.-M. Wu, T. Liu, L. Chen, R. Hao, Y.-J. Song, Y.-P. Liu, Z.-Y. Yuan, Interfacing nickel with molybdenum oxides as monolithic catalyst to accelerate alkaline hydrogen electrocatalysis with robust stability, Appl. Catal. B Environ. 317 (2022) 121786. https://doi.org/10.1016/j.apcatb.2022.121786.

[16] P. Wang, Y. Wang, C. Yuan, B. Chen, T. Zhang, B. Li, Q. Ouyang, Nonlinear absorption, refraction and optical limiting properties of cobalt molybdate microcrystals, Opt. Mater. 124 (2022) 111972. https://doi.org/10.1016/j.optmat.2022.111972.

[17] R. Sasikumar, B. Kim, 3D walnut-like rare-earth gadolinium molybdate encapsulated with thermo-responsive hydrogel for sensitive electrochemical detection of anticancer drug Niftolide in human urine, Colloids Surf. Physicochem. Eng. Asp. 650 (2022) 129593. https://doi.org/10.1016/j.colsurfa.2022.129593.

[18] A. Mobeen Amanulla, SK. Jasmine Shahina, R. Sundaram, C. Maria Magdalane, K. Kaviyarasu, D. Letsholathebe, S.B. Mohamed, J. Kennedy, M. Maaza, Antibacterial, magnetic, optical and humidity sensor studies of β-$CoMoO_4$-Co_3O_4 nanocomposites and its synthesis and characterization, J. Photochem. Photobiol. B. 183 (2018) 233–241. https://doi.org/10.1016/j.jphotobiol.2018.04.034.

[19] F. Davar, M. Salavati-Niasari, Z. Fereshteh, Synthesis and characterization of SnO_2 nanoparticles by thermal decomposition of new inorganic precursor, J. Alloys Compd. 496 (2010) 638–643. https://doi.org/10.1016/j.jallcom.2010.02.152.

[20] M. Ghiyasiyan-Arani, M. Salavati-Niasari, S. Naseh, Enhanced photodegradation of dye in waste water using iron vanadate nanocomposite; ultrasound-assisted preparation and characterization, Ultrason. Sonochem. 39 (2017) 494–503. https://doi.org/10.1016/j.ultsonch.2017.05.025.

[21] S. Duo, Y. Li, H. Zhang, T. Liu, K. Wu, Z. Li, A facile salicylic acid assisted hydrothermal synthesis of different flower-like ZnO hierarchical architectures with optical and concentration-dependent photocatalytic properties, Mater. Charact. 114 (2016) 185–196. https://doi.org/10.1016/j.matchar.2016.02.021.

[22] M. Panahi-Kalamuei, S. Alizadeh, M. Mousavi-Kamazani, M. Salavati-Niasari, Synthesis and characterization of CeO_2 nanoparticles via hydrothermal route, J. Ind. Eng. Chem. 21 (2015) 1301–1305. https://doi.org/10.1016/j.jiec.2014.05.046.

[23] R. Monsef, M. Salavati-Niasari, Hydrothermal architecture of $Cu_5V_2O_{10}$ nanostructures as new electro-sensing catalysts for voltammetric quantification of mefenamic acid in pharmaceuticals and biological samples, Biosens. Bioelectron. 178 (2021) 113017. https://doi.org/10.1016/j.bios.2021.113017.

[24] N. Koga, A. Mako, T. Kimizu, Y. Tanaka, Thermal decomposition of synthetic antlerite prepared by microwave-assisted hydrothermal method, Thermochim. Acta. 467 (2008) 11–19. https://doi.org/10.1016/j.tca.2007.10.016.

[25] A. Phuruangrat, T. Thongtem, S. Thongtem, Synthesis of lead molybdate and lead tungstate via microwave irradiation method, J. Cryst. Growth. 311 (2009) 4076–4081. https://doi.org/10.1016/j.jcrysgro.2009.06.013.

[26] D. Wang, J. Fan, M. Shang, K. Li, Y. Zhang, H. Lian, J. Lin, Pechini-type sol–gel synthesis and multicolor-tunable emission properties of $GdY(MoO_4)_3:RE^{3+}$ (RE=Eu, Dy, Sm, Tb) phosphors, Opt. Mater. 51 (2016) 162–170. https://doi.org/10.1016/j.optmat.2015.11.029.

[27] S. Wang, C. An, Y. Zhang, Z. Zhang, Y. Qian, Ethanothermal reduction to MoO_2 microspheres via modified Pechini method, J. Cryst. Growth. 293 (2006) 209–215. https://doi.org/10.1016/j.jcrysgro.2006.05.007.

[28] S.R. Yousefi, O. Amiri, M. Salavati-Niasari, Control sonochemical parameter to prepare pure $Zn_{0.35}Fe_{2.65}O_4$ nanostructures and study their photocatalytic activity, Ultrason. Sonochem. 58 (2019) 104619. https://doi.org/10.1016/j.ultsonch.2019.104619.

[29] R. Sheng, J. Hu, X. Lu, W. Jia, J. Xie, Y. Cao, Solid-state synthesis and superior electrochemical performance of $MnMoO_4$ nanorods for asymmetric supercapacitor, Ceram. Int. 47 (2021) 16316–16323. https://doi.org/10.1016/j.ceramint.2021.02.211.

[30] Y. Zhao, X. He, R. Chen, Q. Liu, J. Liu, J. Yu, J. Li, H. Zhang, H. Dong, M. Zhang, J. Wang, A flexible all-solid-state asymmetric supercapacitors based on hierarchical carbon cloth@$CoMoO_4$@NiCo layered double hydroxide core-shell heterostructures, Chem. Eng. J. 352 (2018) 29–38. https://doi.org/10.1016/j.cej.2018.06.181.

[31] K.A. Béres, I.E. Sajó, G. Lendvay, L. Trif, V.M. Petruševski, B. Barta-Holló, L. Korecz, F.P. Franguelli, K. László, I.M. Szilágyi, L. Kótai, Solid-Phase "Self-Hydrolysis" of $[Zn(NH_3)_4MoO_4@2H_2O]$ Involving Enclathrated Water—An Easy Route to a Layered Basic Ammonium Zinc Molybdate Coordination Polymer, Molecules. 26 (2021) 4022. https://doi.org/10.3390/molecules26134022.

[32] I.E. Sajó, L.P. Bakos, I.M. Szilágyi, G. Lendvay, J. Magyari, M. Mohai, Á. Szegedi, A. Farkas, A. Jánosity, S. Klébert, L. Kótai, Unexpected Sequential NH_3/H_2O Solid/Gas Phase Ligand Exchange and Quasi-Intramolecular Self-Protonation Yield $[NH_4Cu(OH)MoO_4]$, a Photocatalyst Misidentified before as $(NH_4)_2Cu(MoO_4)_2$, Inorg. Chem. 57 (2018) 13679–13692. https://doi.org/10.1021/acs.inorgchem.8b02261.

[33] Electroanalysis and Biotelectrochemistry Lab, Department of Chemical Engineering and Biotechnology, National Taipei University of Technology, No.1, Section 3, Chung-Hsiao East Road, Taipei 106, Taiwan R.O.C., S. Musuvadhi Babulal, Synthesis of $MnMoO_4$ Nanorods by a Simple Co-Precipitation Method in Presence of Polyethylene Glycol for Pseudocapacitor Application, Int. J. Electrochem. Sci. (2020) 7053–7063. https://doi.org/10.20964/2020.07.90.

[34] Z. Shahri, M. Salavati-Niasari, N. Mir, G. Kianpour, Facile synthesis and characterization of nanostructured flower-like copper molybdate by the co-precipitation method, J. Cryst. Growth. 386 (2014) 80–87. https://doi.org/10.1016/j.jcrysgro.2013.09.031.

[35] H. Liu, D. Zhao, Y. Liu, P. Hu, X. Wu, H. Xia, Boosting energy storage and electrocatalytic performances by synergizing $CoMoO_4$@MoZn22 core-shell structures, Chem. Eng. J. 373 (2019) 485–492. https://doi.org/10.1016/j.cej.2019.05.066.

[36] K. Prasad, G. Rajasekhara Reddy, G. Manjula, S.-H. Park, Y. Suh, B. Purusottam Reddy, K. Mallikarjuna, B. Deva Prasad Raju, Morphological transformation of rod-like to pebbles-like $CoMoO_4$ microstructures for energy storage devices, Chem. Phys. 553 (2022) 111382. https://doi.org/10.1016/j.chemphys.2021.111382.

[37] R. Xue, W. Hong, Z. Pan, W. Jin, H. Zhao, Y. Song, J. Zhou, Y. Liu, Enhanced electrochemical performance of $ZnMoO_4$/reduced graphene oxide composites as anode materials for lithium-ion batteries, Electrochimica Acta. 222 (2016) 838–844. https://doi.org/10.1016/j.electacta.2016.11.045.

[38] H. Lakhlifi, Y. El Jabbar, R. El Ouatib, L. Er-Rakho, B. Durand, S. Guillemet-Fritsch, Synthesis of molybdates $Zn_{1-x}Co_xMoO_4$ ($0 \leq x \leq 1$), by decomposition of the precursors developed by the glycine-nitrate process (GNP), and their characterization, Mater. Sci. Semicond. Process. 114 (2020) 105054. https://doi.org/10.1016/j.mssp.2020.105054.

[39] H. Lakhlifi, M. Benchikhi, R. El Ouatib, L. Er-Rakho, S. Guillemet-Fritsch, B. Durand, Synthesis and physicochemical characterization of pigments based on molybdenum « ZnO-MoO_3: Co^{2+}», (2015) 5.

[40] V.S. Budhiraju, R. Kumar, A. Sharma, S. Sivakumar, Structurally stable hollow mesoporous graphitized carbon nanofibers embedded with $NiMoO_4$ nanoparticles for high performance asymmetric supercapacitors, Electrochimica Acta. 238 (2017) 337–348. https://doi.org/10.1016/j.electacta.2017.04.039.

[41] L. Robertson, M. Duttine, M. Gaudon, A. Demourgues, Cobalt–Zinc Molybdates as New Blue Pigments Involving Co^{2+} in Distorted Trigonal Bipyramids and Octahedra, Chem. Mater. 23 (2011) 2419–2427. https://doi.org/10.1021/cm200795p.

[42] A.S. Jayasree, K.M. Rahulan, R. Annie Sujatha, G. Vinitha, N.A. Little Flower, Influence of Ni doping on the structural and third order nonlinear optical properties of $ZnMoO_4$ nanostructures, Recent Adv. Struct. Funct. Ceram. Dev. Charact. Prop. Appl. 48 (2022) 29267–29273. https://doi.org/10.1016/j.ceramint.2022.05.217.

[43] P. Yadav, E. Sinha, Structural, photophysical and microwave dielectric properties of α-$ZnMoO_4$ phosphor, J. Alloys Compd. 795 (2019) 446–452. https://doi.org/10.1016/j.jallcom.2019.05.019.

[44] Y.-R. Jiang, W.W. Lee, K.-T. Chen, M.-C. Wang, K.-H. Chang, C.-C. Chen, Pechini, J. Taiwan Inst. Chem. Eng. 45 (2014) 207–218. https://doi.org/10.1016/j.jtice.2013.05.007.

[45] L. Aleksandrov, T. Komatsu, R. Iordanova, Y. Dimitriev, Structure study of MoO_3–ZnO–B_2O_3 glasses by Raman spectroscopy and formation of α-$ZnMoO_4$ nanocrystals, Opt. Mater. 33 (2011) 839–845. https://doi.org/10.1016/j.optmat.2011.01.003.

[46] Y. Keereeta, T. Thongtem, S. Thongtem, Effect of medium solvent ratios on morphologies and optical properties of α-$ZnMoO_4$, β-$ZnMoO_4$ and $ZnMoO_4 \cdot 0.8H_2O$ crystals synthesized by microwave-hydrothermal/solvothermal method, Superlattices Microstruct. 69 (2014) 253–264. https://doi.org/10.1016/j.spmi.2014.02.011.

[47] L.S. Cavalcante, E. Moraes, M.A.P. Almeida, C.J. Dalmaschio, N.C. Batista, J.A. Varela, E. Longo, M. Siu Li, J. Andrés, A. Beltrán, A combined theoretical and experimental study of electronic structure and optical properties of β-$ZnMoO_4$ microcrystals, Polyhedron. 54 (2013) 13–25. https://doi.org/10.1016/j.poly.2013.02.006.

[48] R.N. Aljawfi, M.J. Alam, F. Rahman, S. Ahmad, A. Shahee, S. Kumar, Impact of annealing on the structural and optical properties of ZnO nanoparticles and tracing the formation of clusters via DFT calculation, Arab. J. Chem. 13 (2020) 2207–2218. https://doi.org/10.1016/j.arabjc.2018.04.006.

[49] G.D. Saraiva, W. Paraguassu, A.J.R. de Castro, F.F. de Sousa, J.G. da Silva Filho, V.O.S. Neto, J.A. Lima, A.M.R. Teixeira, P.T.C. Freire, Lattice dynamics calculations and high-pressure Raman spectra of the $ZnMoO_4$, Spectrochim. Acta. A. Mol. Biomol. Spectrosc. 239 (2020) 118501. https://doi.org/10.1016/j.saa.2020.118501.

[50] X. Xing, X. Xu, J. Wang, W. Hu, Preparation and inhibition behavior of $ZnMoO_4$/reduced graphene oxide composite for Q235 steel in NaCl solution, Appl. Surf. Sci. 479 (2019) 835–846. https://doi.org/10.1016/j.apsusc.2019.02.149.

[51] V. Jeseentharani, A. Dayalan, K.S. Nagaraja, Co-precipitation synthesis, humidity sensing and photoluminescence properties of nanocrystalline Co^{2+} substituted zinc(II)molybdate ($Zn_{1-x}Co_xMoO_4$; x = 0, 0.3, 0.5, 0.7, 1), Solid State Sci. 67 (2017) 46–58. https://doi.org/10.1016/j.solidstatesciences.2017.02.008.

[52] H. Lakhlifi, Y. El Jabbar, S. Guillemet-Fritsch, B. Durand, L. Er-Rakho, R. El Ouatib, Purple nanometrics pigments based on cobalt-doped manganese molybdate: Synthesis, characterization, structural, thermal, optical, colorimetric and chemical properties, J. Mol. Struct. 1248 (2022) 131458. https://doi.org/10.1016/j.molstruc.2021.131458.

[53] H. Lakhlifi, Y.E. Jabbar, R. El Ouatib, L. Er-Rakho, S. Guillemet-Fritsch, B. Durand, Structural, morphological and optical properties of cobalt-substituted $MgMoO_4$ ceramics prepared by pyrolysis of citric acid precursors, Surf. Interfaces. 21 (2020) 100718. https://doi.org/10.1016/j.surfin.2020.100718.

[54] N. Padmanathan, H. Shao, S. Selladurai, C. Glynn, C. O'Dwyer, K.M. Razeeb, Pseudocapacitance of α-$CoMoO_4$ nanoflakes in non-aqueous electrolyte and its bi-functional electro catalytic activity for methanol oxidation, Int. J. Hydrog. Energy. 40 (2015) 16297–16305. https://doi.org/10.1016/j.ijhydene.2015.09.127.

[55] H. Lakhlifi, Y. El Jabbar, M. Benchikhi, L. Er-Rakho, B. Durand, R. El Ouatib, Nanocrystalline transition metal ($CoMoO_4$) prepared by sol gel method: Correlation between powder colors and α/β phase transformations, Inorg. Chem. Commun. (2022) 110049. https://doi.org/10.1016/j.inoche.2022.110049.

[56] H. Chen, H. Hu, F. Han, J. Liu, Y. Zhang, Y. Zheng, $CoMoO_4$ /bamboo charcoal hybrid material for high-energy-density and high cycling stability supercapacitors, Dalton Trans. 49 (2020) 10799–10807. https://doi.org/10.1039/D0DT00147C.

[57] M. Benchikhi, R. El Ouatib, S. Guillemet-Fritsch, J. Yves Chane-Ching, L. Er-Rakho, B. Durand, Sol–gel synthesis and sintering of submicronic copper molybdate (α-$CuMoO_4$) powders, Ceram. Int. 40 (2014) 5371–5377. https://doi.org/10.1016/j.ceramint.2013.10.118.

[58] S. Laufer, S. Strobel, T. Schleid, J. Cybinska, A.-V. Mudring, I. Hartenbach, Yttrium(iii) oxomolybdates(vi) as potential host materials for luminescence applications: an investigation of Eu^{3+}-doped $Y_2[MoO_4]_3$ and $Y_2[MoO_4]_2[Mo_2O_7]$, New J. Chem. 37 (2013) 1919. https://doi.org/10.1039/c3nj00166k.

[59] V. Sasca, A. Popa, Band-gap energy of heteropoly compounds containing Keggin polyanion-$[PV_xMo_{12-x}O_{40}]^{(3+x)-}$ relates to counter-cations and temperature studied by UV-VIS diffuse reflectance spectroscopy, J. Appl. Phys. 114 (2013) 133503. https://doi.org/10.1063/1.4820582.

[60] I.S. Altarawneh, S.E. Rawadieh, M.A. Batiha, L.A. Al-Makhadmeh, M.A. Al-Shaweesh, M.K. Altarawneh, Structures and thermodynamic stability of cobalt molybdenum oxide ($CoMoO_4$-II), Surf. Sci. 677 (2018) 52–59. https://doi.org/10.1016/j.susc.2018.05.018.

[61] A. Jezierski, Electronic and magnetic properties of $Cu_2MgV_2O_8$ and $CuMg_2V_2O_8$–ab initio study, Solid State Commun. 314–315 (2020) 113943. https://doi.org/10.1016/j.ssc.2020.113943.

[62] M. Ullah, A.M. Rana, U. Mehtab, M. Farooq, Study of structural, electronic and optical properties of co-doped CeO_2 using the density functional theory (DFT) method, Mater. Sci. Semicond. Process. 130 (2021) 105800. https://doi.org/10.1016/j.mssp.2021.105800.

[63] A. Natik, Y. Abid, R. Moubah, M. Abid, H. Lassri, Ab-initio investigation of the structural, electronic and optical properties of lead-free halide Cs_2TiI_6 double perovskites, Solid State Commun. 319 (2020) 114006. https://doi.org/10.1016/j.ssc.2020.114006.

[64] M. Bouhbou, R. Moubah, K. Bakkari, H. Zaari, A. Sabrallah, F. Khelfaoui, N. Mliki, M. Abid, A. Belayachi, H. Lassri, Magnetic, half-metallicity and electronic studies of $Cd_{1-x}Zn_xCr_2Se_4$ chromium selenospinels, J. Magn. Magn. Mater. 476 (2019) 86–91. https://doi.org/10.1016/j.jmmm.2018.12.063.

[65] M.C. Viola, M.J. Martínez-Lope, J.A. Alonso, P. Velasco, J.L. Martínez, J.C. Pedregosa, R.E. Carbonio, M.T. Fernández-Díaz, Induction of Colossal Magnetoresistance in the Double Perovskite Sr_2CoMoO_6, Chem. Mater. 14 (2002) 812–818. https://doi.org/10.1021/cm011186j.

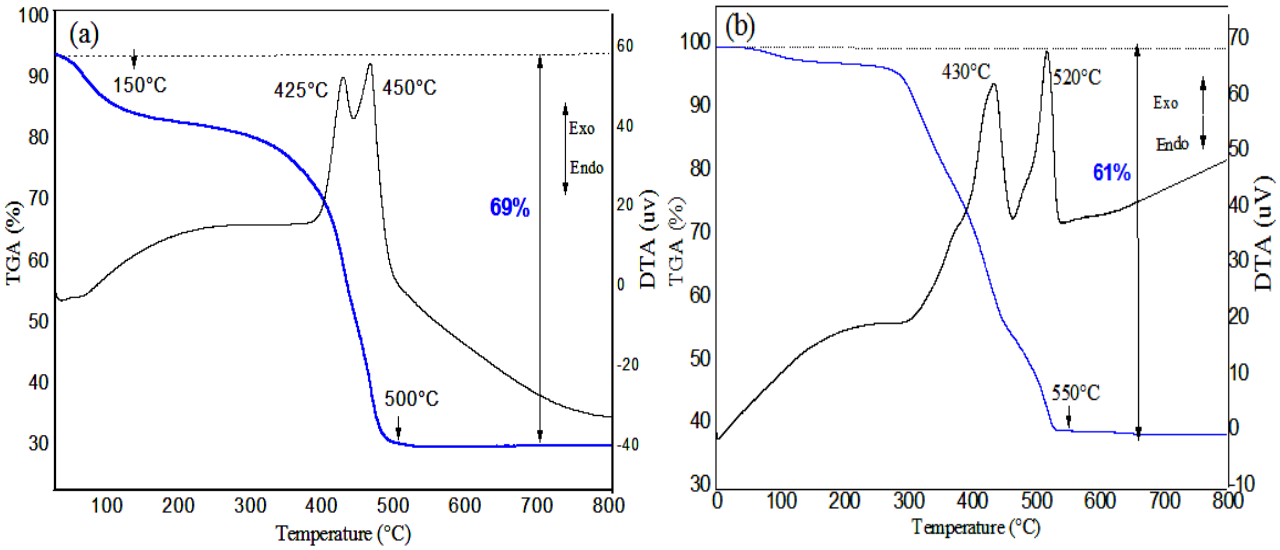

Fig. 1. TGA-DTA analysis of dried gel of (*a*): ZnCoMo-0.3-300 and (*b*): ZnCoMo-0.6-300 precursors.

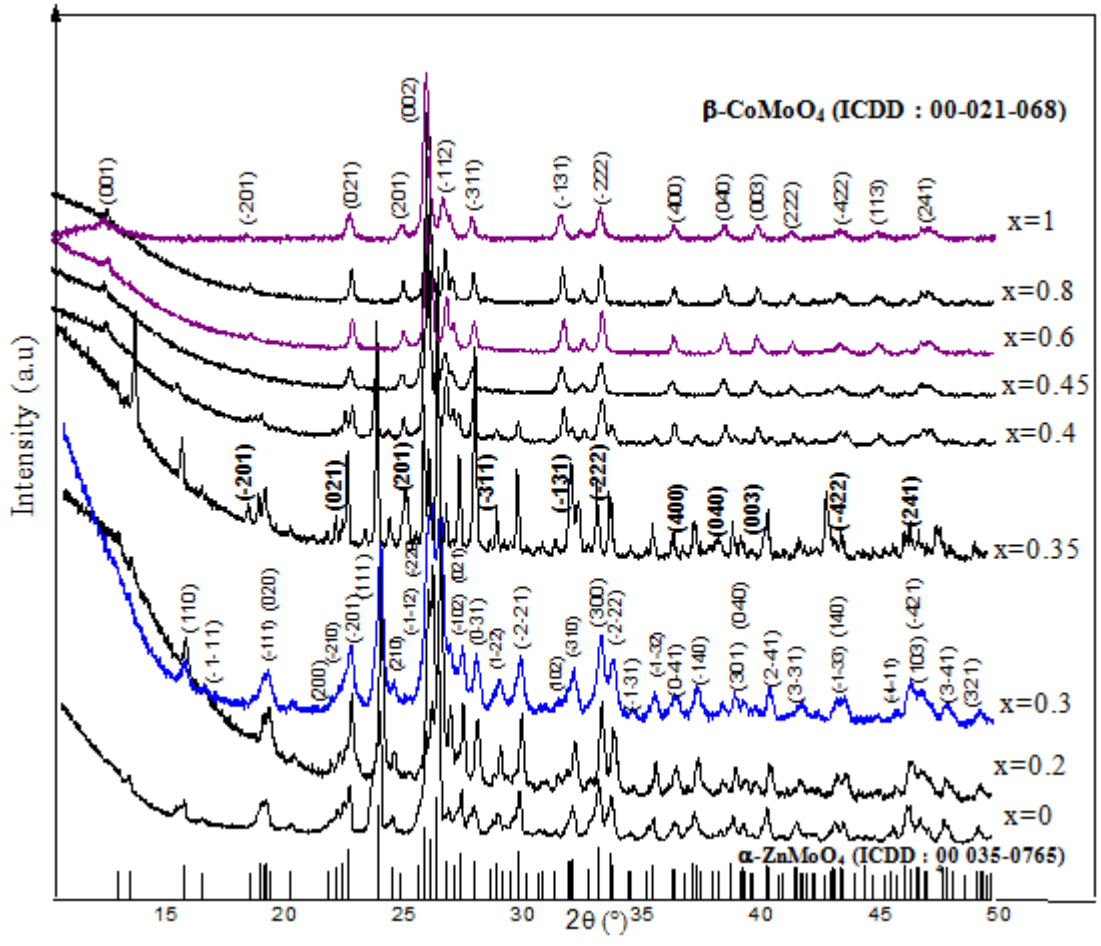

Fig. 2a. X-ray diffraction patterns of ZnCoMo-x-600 ($0 \leq x \leq 1$) compounds prepared at 600 °C (without grinding).

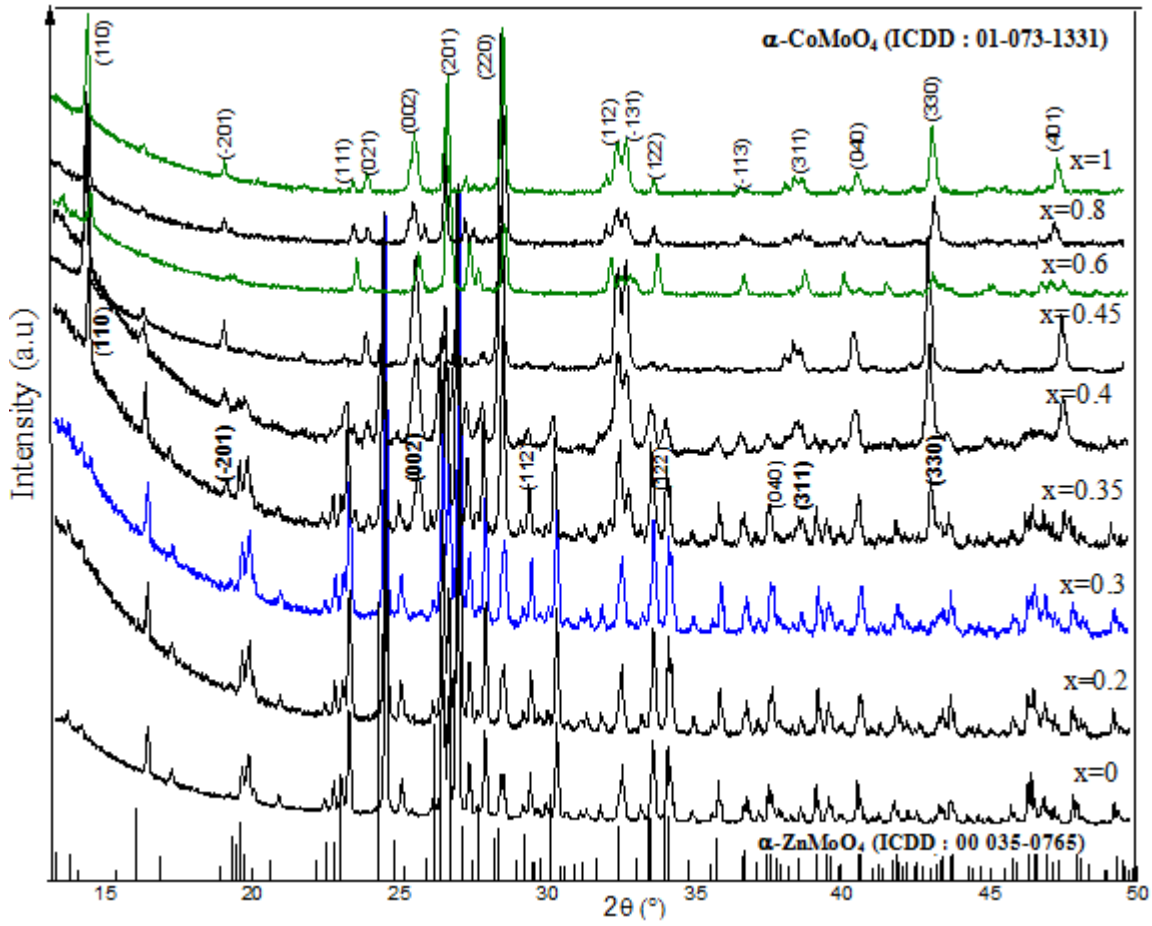

Fig. 2b. X-ray diffraction patterns of ZnCoMo-x-600 ($0 \leq x \leq 1$) compounds prepared at 600 °C (with grinding).

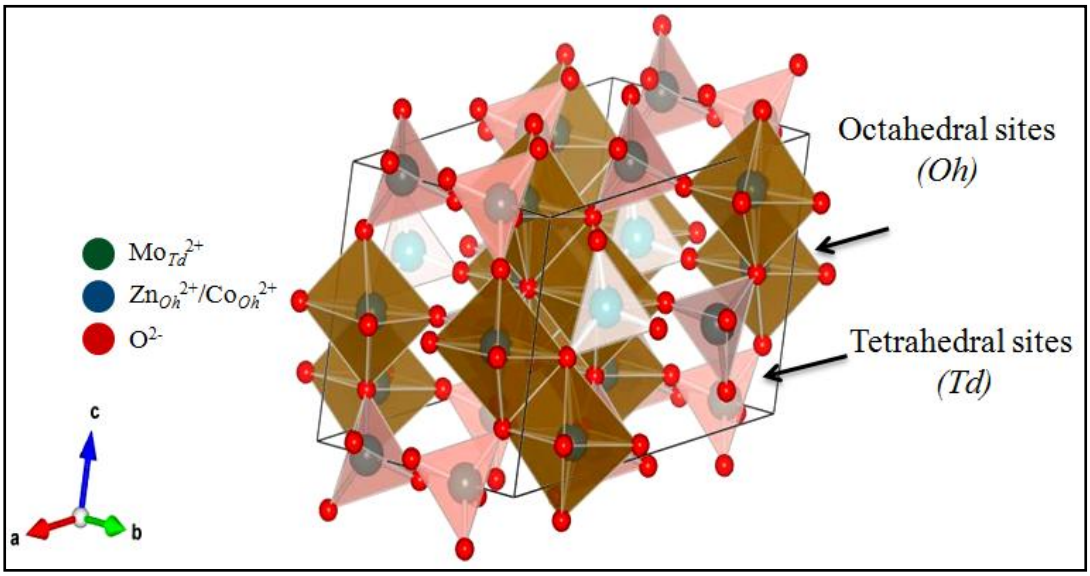

Fig. 2c. Ball and stick representation of crystal structure of the ZnCoMo-0.3-600 nanocrystalline powder.

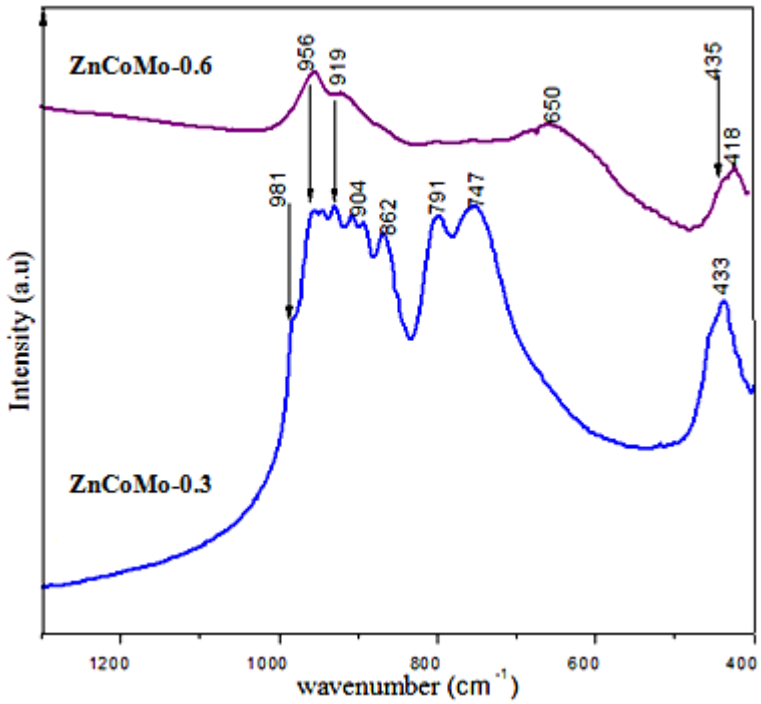

Fig. 3. FT-IR spectra of the ZnCoMo-0.3-600 and ZnCoMo-0.6-600 powders.

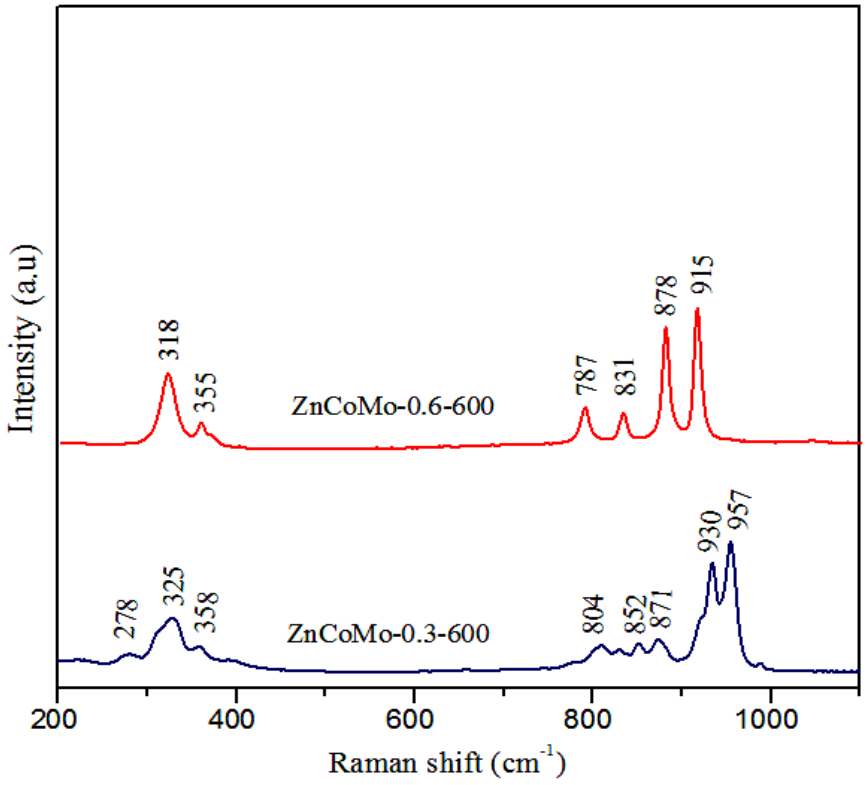

Fig.4. Raman Spectra of the ZnCoMo-0.3-600 and ZnCoMo-0.6-600 molybdates.

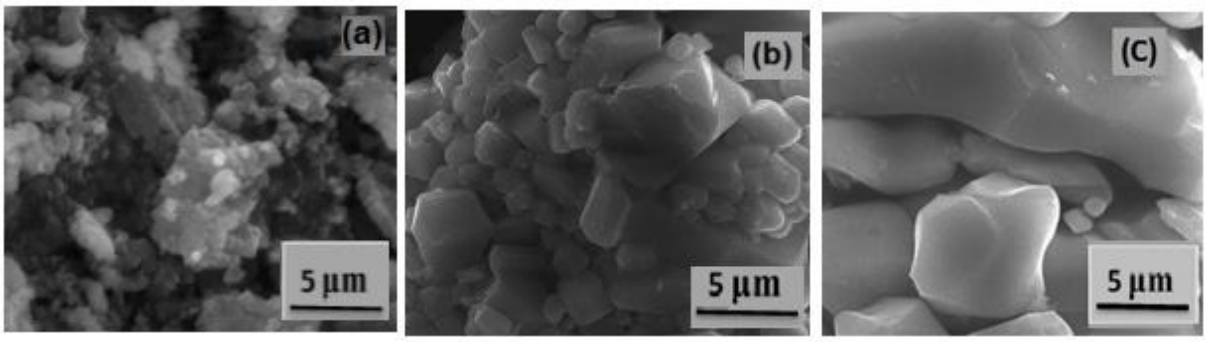

Fig. 5a. SEM micrographs of ZnCoMo-0.3-T powder obtained at: (*a*) 600 °C, (*b*) 700 °C and (*c*) 800 °C.

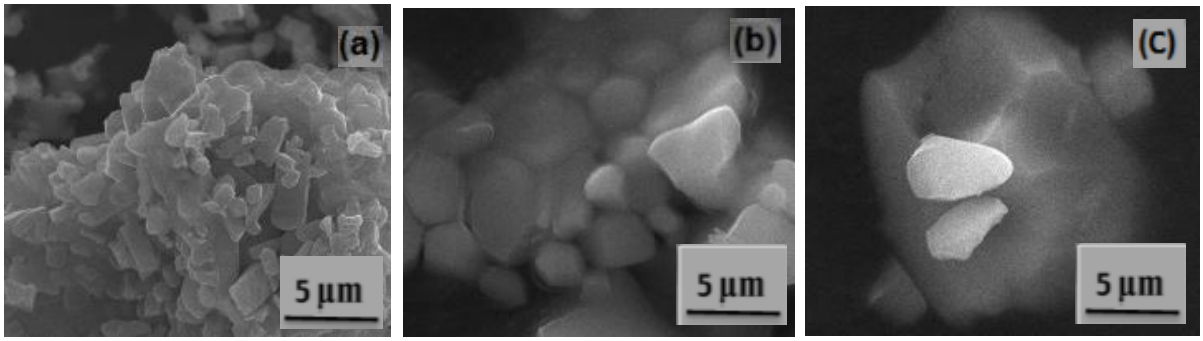

Fig.5b. SEM micrographs of ZnCoMo-0.6-T powder obtained at: (*a*) 600 °C, (*b*) 700 °C and (*c*) 800 °C.

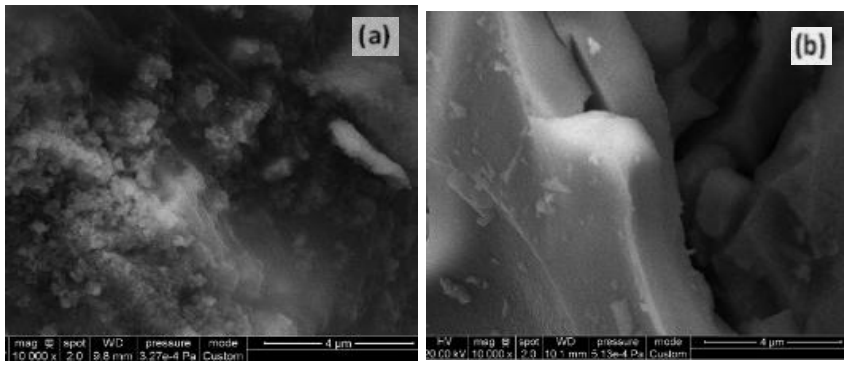

Fig. 5c. SEM -FEG micrographs of ZnCoMo-0.3-T powder obtained at: (*a*) 700 °C and (*b*) 800 °C.

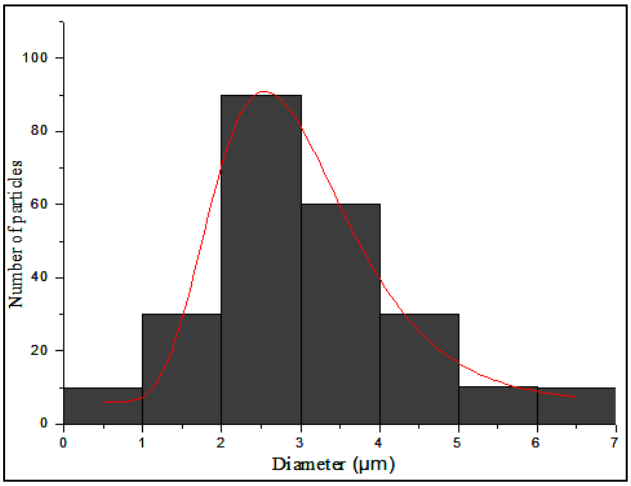

Fig. 6. Particle sizes distribution calculated from multiple SEM images of ZnCoMo-0.3-700 powder.

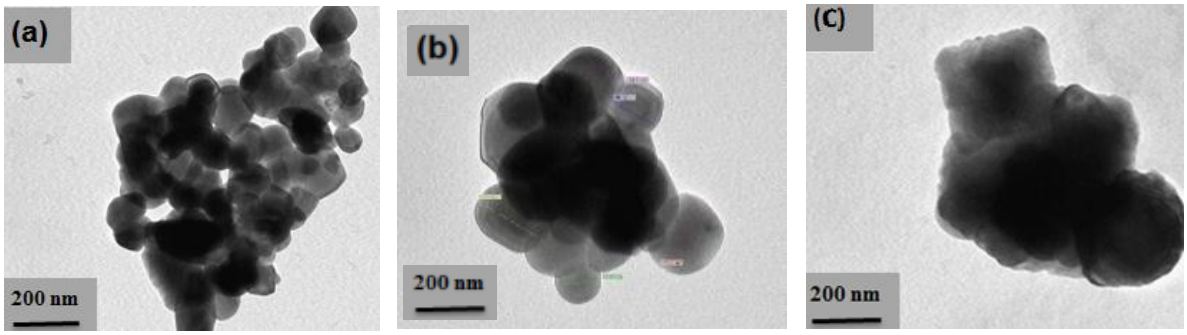

Fig. 7. TEM micrographs of ZnCoMo-0.3-T powder prepared in acid medium at: (*a*) 600 °C, (*b*) 700 °C and (*c*) 800 °C.

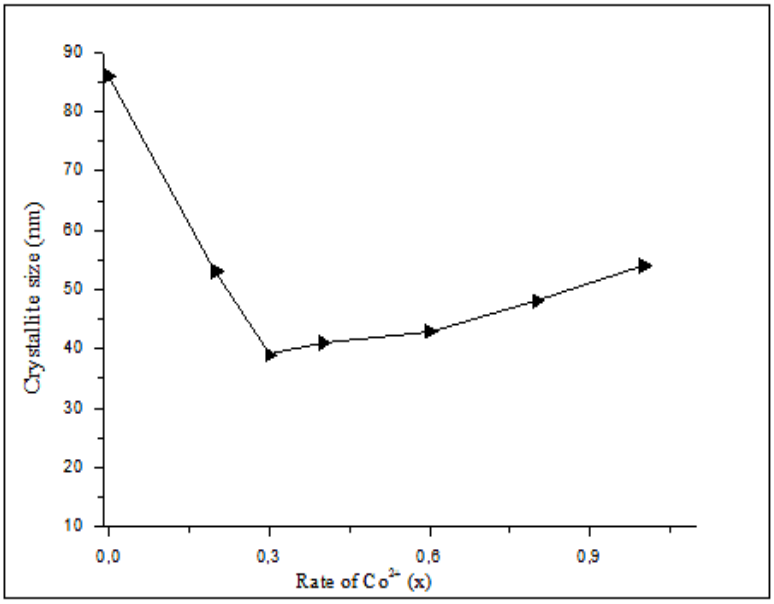

Fig. 8. Evolution and growth of crystallite size of ZnCoMo-x-600 compounds deduced from the Scherrer equation using XRD line broadening, as a function of Co^{2+} (x) rates $0 \leq x \leq 1$.

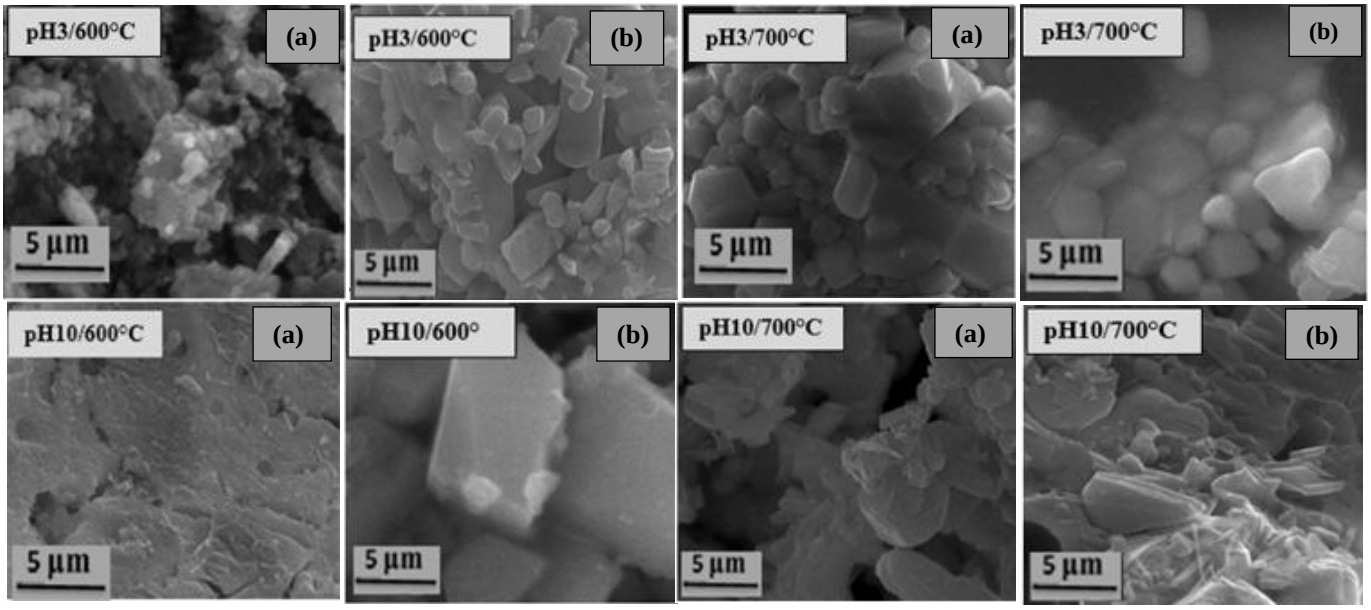

Fig. 9. SEM micrographs of (a) ZnCoMo-0.3-T and (b) ZnCoMo-0.6-T compounds synthesized in acid and basic pH at 600 and 700 °C.

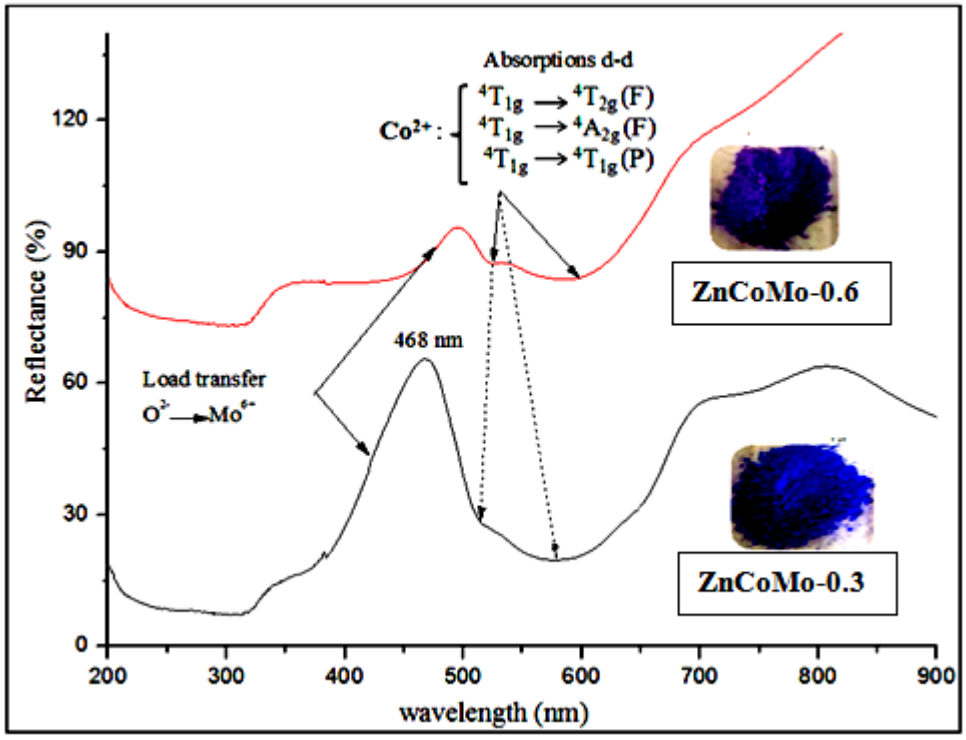

Fig. 10. Shades of the blue/purple colors and diffuse reflectance spectra of ZnCoMo-0.3-700 and ZnCoMo-0.6-700 powders.

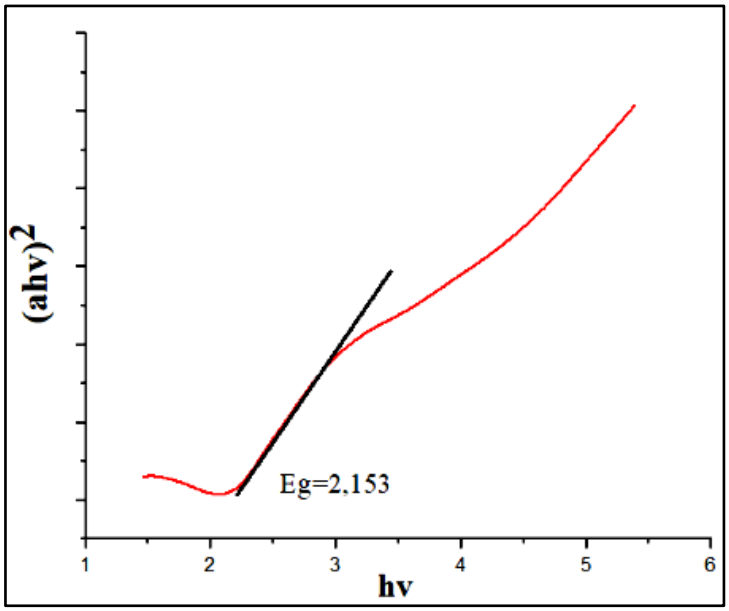

Fig. 11. Plot of $(h\upsilon\alpha)^2$ as a function of hυ (direct transition) of molybdate ZnCoMo-1-700.

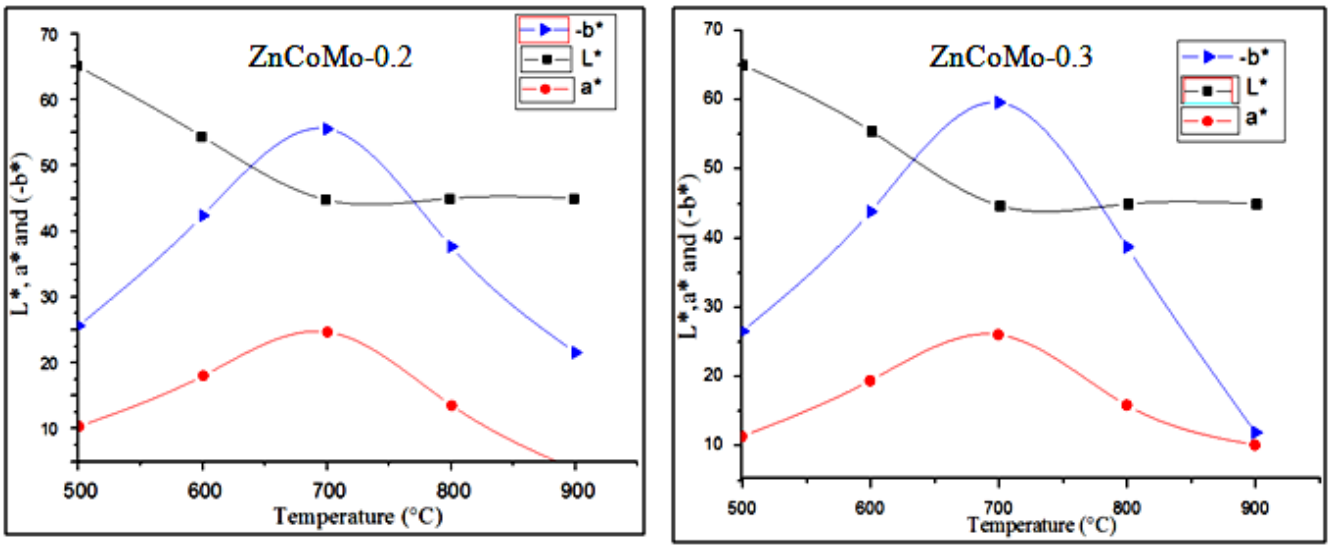

Fig. 12. Evolution of the color parameters of ZnCoMo-0.2-T and ZnCoMo-0.3-T pigments as a function of temperature.

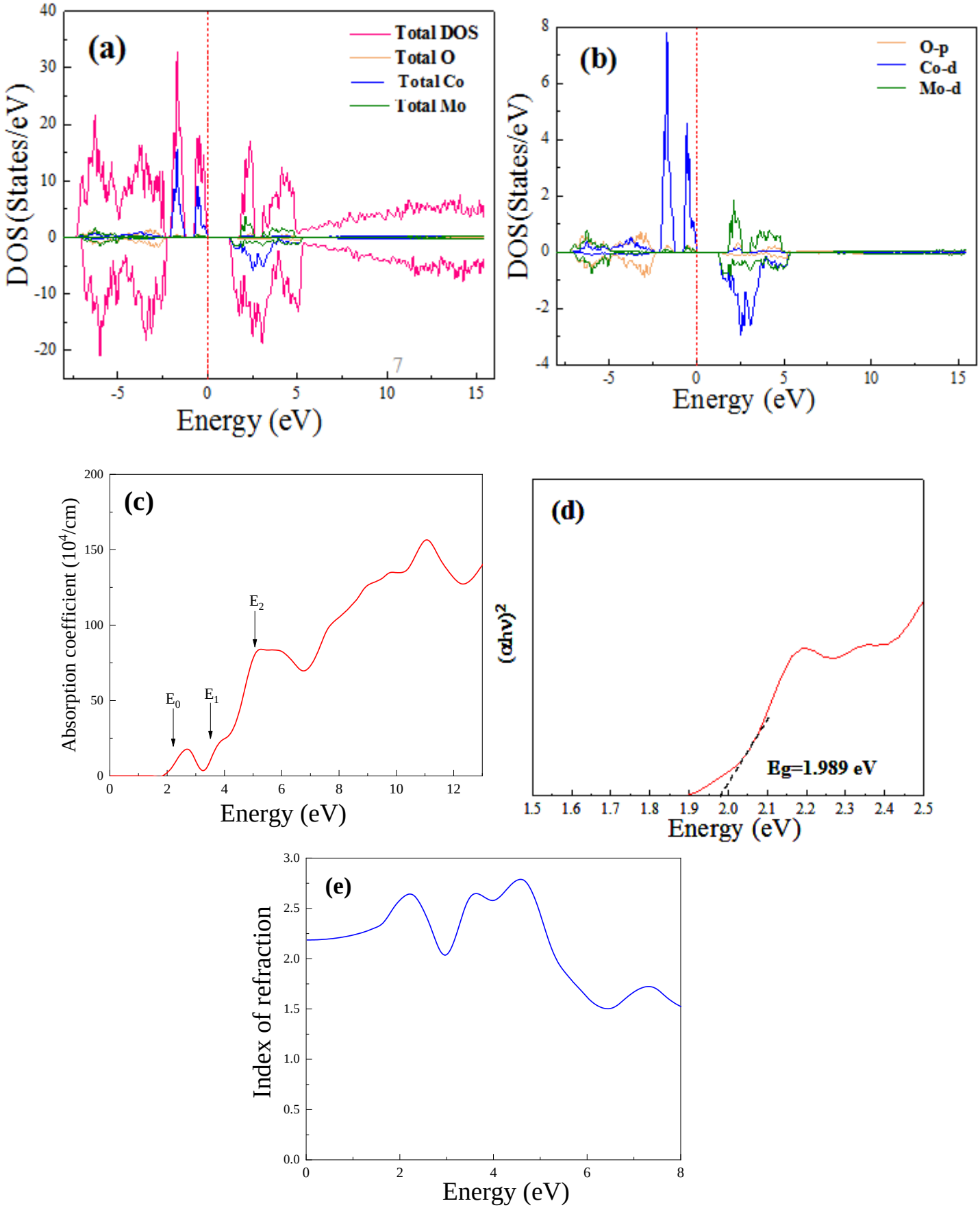

Fig. 13. (*a*) Total density of states (DOS), (*b*) partial density of states (PDOS), (*c*) absorption spectrumof the ZnCoMo-1-700 (β-$CoMoO_4$), (*d*) $(\alpha h\upsilon)^2$ plots and (*e*) index of refraction.

Table 1

Specific surface area measurements for ZnCoMo-0.3-T and ZnCoMo-0.6-T powders at different temperature.

T (◦C)	Specific surface area (m^2/g)		
	***x* = 0.3**	***x* = 0.6**	***x* = 1**
600 °C	56.7	49.5	42.3
700 °C	47.5	38.7	34.2
800 °C	33.9	21.8	17.5

Table 2

Grain size of ZnCoMo-0.3-600 and ZnCoMo-0.6-600 powders prepared in acid and basic medium.

Cobalt content	pH	XRD crystallite size (nm)
ZnCoMo-0.3-600	3	53
	10	89
ZnCoMo-0.6-600	3	62
	10	51

Table 3

Optical band gaps (E*g*) of ZnCoMo-x-700 (x= 0, 0.3, 0.6 and 1) powders.

Samples	Band gap E*g* (eV)
ZnCoMo-0-700	4.03
ZnCoMo-0.3-700	3.28
ZnCoMo-0.6-700	2.47
ZnCoMo-1-700	2.15

Table 4

Magnetic moments and band gap of sample ZnCoMo-1-700 (β-$CoMoO_4$).

β-$CoMoO_4$						
$Eg_{(theorical)}$ **(*eV*)**	$Eg_{(experimental)}$ **(*eV*)**	$\mu_{(Co)}$	$\mu_{(Mo)}$	$\mu_{(O)}$	$\mu_{(theorical)}$ **(μ_B)**	$\mu_{(experimental)}$ **(μ_B) [65]**
1.989	2.153	4.30904	0.11072	0.05844	5.00049	5.20